

Time-resolved and three-dimensional elucidation of the complex refractive index alteration induced by ultrashort laser pulses

Takumi Koike*, Yusuke Ito, Naohiko Sugita

Department of Mechanical Engineering, School of Engineering, The University of Tokyo, Bunkyo-ku, Tokyo 113-8656, Japan

*Corresponding author: t.koike@mfg.t.u-tokyo.ac.jp (Takumi Koike)

Abstract

Ultrashort pulse lasers (USPLs) have garnered attention as a tool that is capable of inducing a variety of unique phenomena by instantaneously inducing a region of altered physical properties (filaments) in the material. However, a comprehensive understanding of the USPL-induced filaments has remained elusive due to the complexity of the dynamics involved and the lack of imaging technology to accurately extract such dynamics. In this study, we propose a novel methodology for measuring the transient properties, i.e., the complex refractive index of the filament through analysis of the polarization state of the probing pulse. Our proposed methodology was successful in the accurate extraction of three-dimensional distribution of complex refractive index that fluctuates ultrafast, for the first time to our knowledge. Our work will provide insights into the complex ablation mechanisms incurred by USPLs, which are critical in selecting optimal laser conditions in micro/nano processing. The findings of this study will also make significant contributions to the fields of condensed matter and computational physics through precise actual data on the physical property of the USPL-irradiated region.

Introduction

Transparent insulators are essential components in precision electronics, medical devices, and other sophisticated equipment [1-3]. The ultrashort pulse laser (USPL) has garnered attention as a tool for processing such materials with high precision [4, 5]. One of the reasons that USPL enables such processing is that its irradiation instantly induces metallic regions (filaments) in the material, thereby converting the irradiated material to an easily machinable state. The behavior of such filaments has been a subject of interest in various fields, including precision engineering and condensed matter/computational physics, since their initial discovery in the late 20th century [6-10]. Therefore, the development of an accurate measurement technique for the complex refractive indices of filaments could provide a solution to the industrial and academic questions surrounding filament

behavior.

However, despite this need, existing techniques are limited in their ability to fulfill this purpose. For instance, shadowgraphy, a method employed to measure the imaginary part of the refractive index [11], is incapable of measuring the real part, and its measurement results are highly dependent on the intensity of the observation light. Interferometry, a technique for measuring the real part [12], requires meticulous experimental techniques to induce optical interference at the observation point, making it susceptible to errors in the measurement results. Several attempts have been made to capture all components of the refractive index, such as pseudorecovery by combining the above two (or equivalent) methods, still with limited success due to the difficulty in capturing exactly the same moment via different methods. In terms of capturing all components of the complex refractive index, ellipsometry has demonstrated some success [13]. This method, however, is not applicable to filaments since the analysis by this method basically relies on the probing light reflected from the material surface, which is unable to analyze the internal properties. While several examples have used transmitted probes for ellipsometry, to our knowledge, there are no examples of utilizing this method to analyze microstructures such as filaments.

Here, we propose a novel method that enables an accurate measurement of filaments by analyzing the polarization state of the observation light transmitted through the object. This approach has enabled the precise extraction of the spatio-temporal evolution of all components of the complex refractive index of the filament for the first time to our knowledge. The results showed reasonable agreement with both conventional measurements and numerical calculations, confirming the accuracy of our approach.

Results

Concept of Proposed Method

The experimental configuration shown in Fig. 1 was designed to analyze the polarization state of the observation pulse transmitted through the filament. A single USPL emitted from the amplifier in the setup was split into two branches: one (processing pulse) was utilized to generate the filament in the sample, while the other (observation pulse) was employed to observe the high-speed phenomena induced by the former. The temporal separation between the two pulses is established by a motor-controlled optical delay, thus performing the time-resolved measurement. With a fixed optical delay, a series of images were obtained while systematically varying the polarizer angle from 0° to 180° (see Appendix. 1 for details). This operation enabled the measurement of the light intensity behavior as a function of the angle display α of the rotating polarizer, at a fixed time delay

after the start of filament formation. In the following, this experimentally-obtained light intensity behavior distribution is referred to as $\iota(\alpha)$ (see Fig. 2). A comprehensive exposition of the experimental conditions can be found in Table 1.

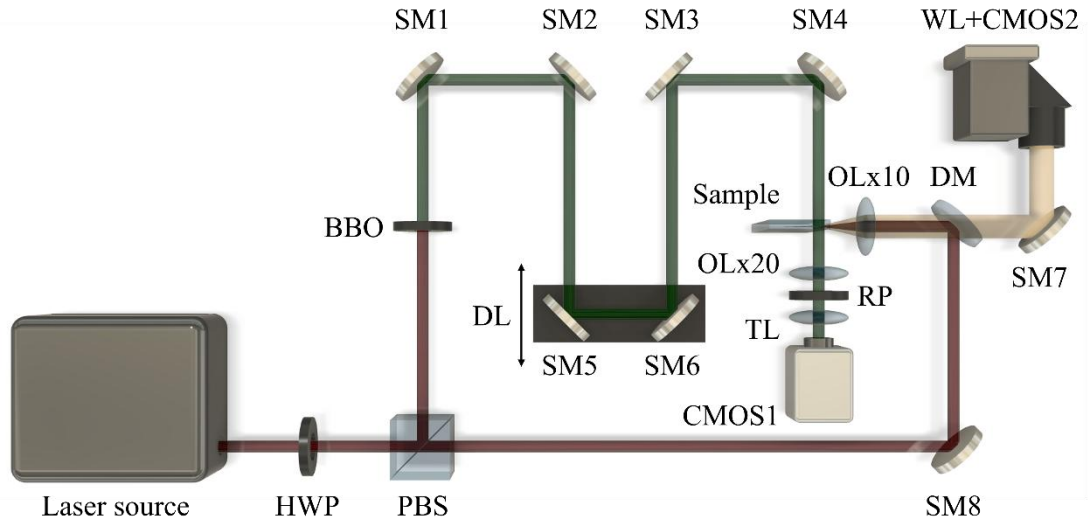


Fig. 1 Schematic of the experimental setup. HWP: half-wave plate; PBS: polarizing beam splitter; BBO: beta barium borate crystal; SM: silver mirror; DL: motor-controlled optical delay line; DM: dichroic mirror; OLx10/x20: objective lens; TL: tube lens; CMOS1: BH-73M, Bitran; CMOS2: DCC1645C-HQ, Thorlabs; WL: white light. The sample position was identified by positioning where the reflected white light, illuminated on the sample surface, was focused on CMOS2.

Table 1 Experimental conditions

Sample	Silica glass
Pulse energy	100 μ J
Pulse duration	2 ps
Focal position	100 μ m under surface

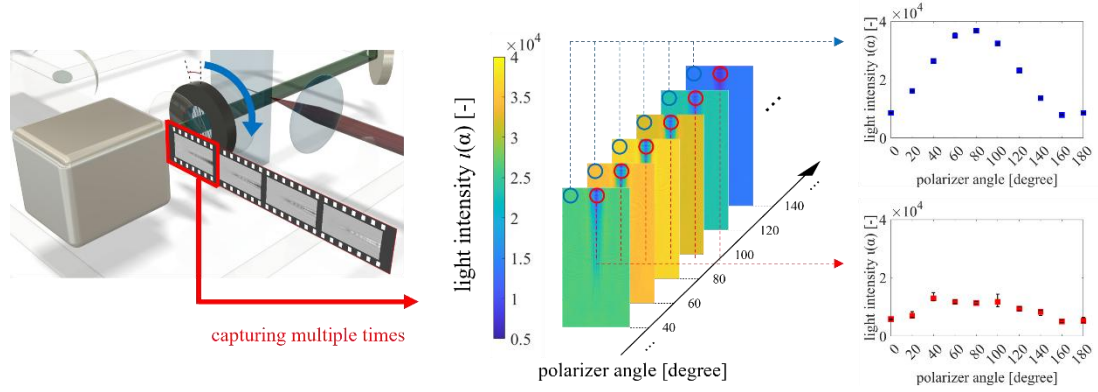


Fig. 2 Schematic of the light intensity measurement method. With the optical delay fixed, filament images are recorded while rotating the polarizer positioned in front of the imaging device (left). This enables the measurement of the intensity profile $I(\alpha)$ as a function of the polarizer angle at each pixel (right).

The behavior of the recorded light intensity $I(\alpha)$ can theoretically be expressed by $I(\alpha)$ (see Eq. (2)). This expression is derived by squaring the absolute value of the electric field $E(\alpha)$, which is obtained through Jones calculus (Eq. (1): see Appendix. 2 for a concise derivation). In this equation, θ denotes the angle that the transmission axis of the rotating polarizer makes with the vertical axis when the angle display is at the origin. The remaining parameters (Ψ , Δ , ψ , and δ) are employed to describe the polarization state of the observation pulse: the first two describe the polarization state change after propagation through the filament, while the last two parameters describe the initial polarization state. The values of these parameters can all be estimated by identifying the representation of $I(\alpha)$ that yields the closest fit to $I(\alpha)$ using the least squares approximation method (see Appendix.3 for details).

$E(\alpha)$

$$\propto \begin{bmatrix} 0 & 0 \\ 0 & 1 \end{bmatrix} \begin{bmatrix} \cos(\alpha + \theta) & \sin(\alpha + \theta) \\ -\sin(\alpha + \theta) & \cos(\alpha + \theta) \end{bmatrix} \begin{bmatrix} \sin \Psi \exp(-j\Delta) & 0 \\ 0 & \cos \Psi \end{bmatrix} \times \begin{bmatrix} \sin \psi \exp(-j\delta) \\ \cos \psi \end{bmatrix} \quad (1)$$

$$= \begin{bmatrix} 0 \\ -\sin \Psi \sin \psi \exp(-j(\Delta + \delta)) \sin(\alpha + \theta) + \cos \Psi \cos \psi \cos(\alpha + \theta) \end{bmatrix},$$

$I(\alpha)$

$$= A |E(\alpha)|^2 \quad (2)$$

$$= A |-\sin \Psi \sin \psi \exp(-j(\Delta + \delta)) \sin(\alpha + \theta) + \cos \Psi \cos \psi \cos(\alpha + \theta)|^2$$

The definition of the above-mentioned polarization parameters (Ψ and Δ) is provided in Eq(3): these parameters are employed to express the amplitude ratio and phase difference of each polarization component of the transmitted observation light [14]. The changes in these parameters are induced by the complex refractive index distribution near the filament. Utilizing this relation, the complex refractive index in question can be determined from the polarization parameters, whose values have already been determined.

$$\tan \Psi \exp(-j\Delta) \equiv \frac{t_P}{t_S} \quad (3)$$

Figure 3 schematically illustrates this relation. Panel (a) presents the geometric relationship between the filament and the observation pulse, with the radial direction denoted by the r axis and the axial direction by the z axis. This representation is based on the reasonable assumption that the filament is axially symmetric, since the intensity profile of the USPL that induces the filament follows a Gaussian distribution. The primary factor responsible for this polarization state change is the inhomogeneity in the refractive index. Contributing phenomena include Fresnel effects, multiple internal reflections at refractive index boundaries, and birefringence [14]. Among these, the effects of Fresnel refractions and multiple internal reflections are known to be negligible in absorptive media [15] or in media with gradually varying refractive indices (see Appendix 4). Therefore, birefringence is considered the dominant contributor in the present analysis.

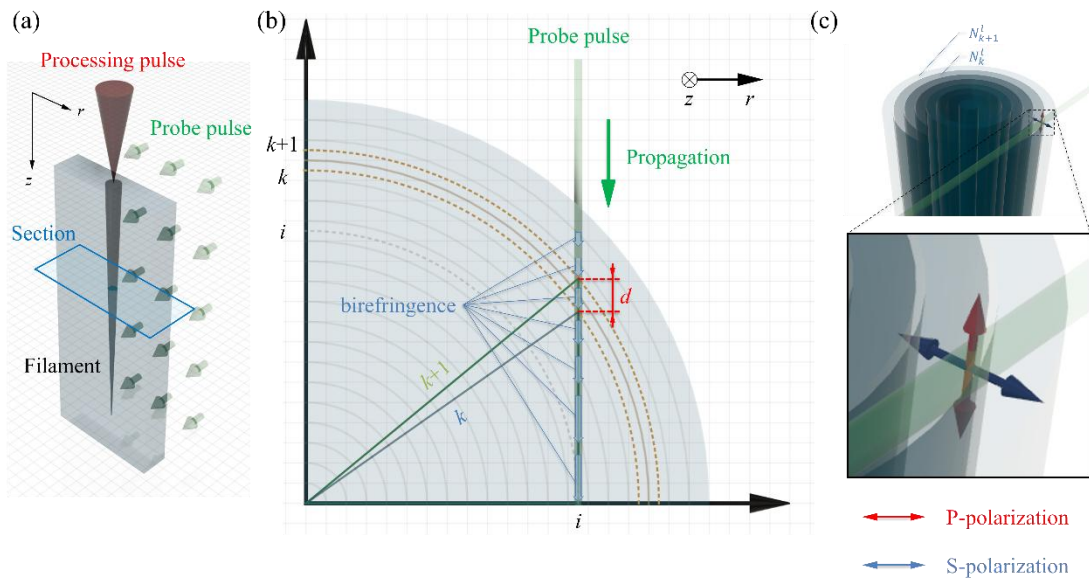


Fig. 3 Relationship between the USPL-induced filament and the polarization state change of the probe pulse. (a) Perspective view, (b) Cross-sectional view at $z = l$, and (c) Refractive index distribution for each polarization direction.

The effect of birefringence can be described as follows [16-18]:

$$\begin{aligned}
& \delta \frac{t_P}{t_S} \Big|_{r=k \sim k+1}^{z=l} \\
&= \delta \{ \tan \Psi \exp(-j\Delta) \} \Big|_{r=k \sim k+1}^{z=l} \\
&= \exp \left\{ \frac{2\pi j d}{\lambda} (n_P - n_S) \right\}
\end{aligned} \tag{4}$$

This equation describes the complex transmittance ratio change (and therefore the polarization state change; see Eq.(3)) induced in the observation pulse that intersects at $r = i$, as it propagates through concentric refractive index layers from $r = k+1$ to $r = k$ (see Fig. 3(b)). Here, d denotes the spacing between the two concentric layers, λ is the wavelength, n_P and n_S are the refractive indices for the P- and S-polarized components, respectively, and j is an imaginary unit. Note that the symbol δ signifies a minor alteration in the physical quantity, and is unrelated to the polarization parameter δ . Under these configurations, the S- and P-polarization directions are respectively oriented horizontally and in-plane (see Fig. 3(b)). Accordingly, n_S and n_P can be identified with N_{k+1}^l and N_k^l , respectively (see Fig. 3(c)), and therefore Eq. (4) can be reformulated as Eq. (5), where N_k^l denotes the refractive index at the coordinate $(r, z) = (k, l)$.

$$\exp \left\{ \frac{2\pi j d}{\lambda} (n_P - n_S) \right\} = \exp \left\{ \frac{2\pi j d_k^i}{\lambda} (N_k^l - N_{k+1}^l) \right\}$$

where

$$d_k^i \equiv \begin{cases} \sigma \left(\sqrt{(k+1)^2 - i^2} - \sqrt{k^2 - i^2} \right) \cdots & \text{for } k \geq i + 1 \\ \sigma \sqrt{2i + 1} \cdots & \text{for } k = i \end{cases} \tag{5}$$

Here, σ denotes the pixel length in the image, and d_k^i is the effective spacing between the concentric layers as viewed from the observation coordinate $r = i$, determined by straightforward geometric consideration.

The cumulative change in polarization state after passing through all concentric layers can be expressed as the product of individual contributions at each position. This is specifically expressed by Eq. (6), where i_{\max} is the r -axis endpoint coordinate in the imaging area.

$$\tan \Psi \exp(-j\Delta)|_{r=i}^{z=l} = \prod_{k=i}^{i_{max}} \left[\exp \left\{ \frac{2\pi d_k^i j}{\lambda} (N_k^l - N_{k+1}^l) \right\} \right]^2 \quad (6)$$

Utilizing Eq.(6), the complex refractive index near the filament can be obtained. A detailed explanation of this procedure is provided in Appendix. 5.

Spatiotemporal Evolution of Polarization Parameters

Figures 4(a)–(c) present the experimental results of the polarization parameters in conjunction with the corresponding filaments induced by 2-ps USPLs. Figures 4(a) and 4(b) depict the spatial distributions of the polarization parameters Ψ and Δ , respectively, while Fig. 4(c) displays the associated filament images obtained via shadowgraphy. A common trend across these results is that, at locations distant from the filament region, the polarization parameters approximate the baseline values of $(\Psi, \Delta) = (45^\circ, 0^\circ)$, hereafter referred to as the ground-state values. In contrast, pronounced deviations from these values are observed in the vicinity of the filaments. This indicates that the proposed method successfully captures spatial regions where the polarization state deviates from the ground state, with a distribution that closely resembles the filament.

To enable a more quantitative evaluation, Figs. 5(a)–(c) show the temporal evolution of the polarization parameters and transmittance along the central axis of the same filaments. Each plot is color-coded according to the elapsed time following USPL irradiation: red, magenta, green, and blue represent 2, 10, 100, and 500 ps, respectively. A cross-comparison of data with identical color coding across the figures reveals a clear correlation: greater deviation of the polarization parameters from their ground-state values is associated with lower transmittance. Furthermore, the intra-figure temporal progression (i.e., color-coded data within each graph) reveals that both transmittance and the polarization parameters gradually return to their ground-state values with increasing time after irradiation (Figs. 5(a)–(c)). These findings are consistent with the interpretation that USPL-induced refractive index inhomogeneities perturb the polarization state [13], and that subsequent relaxation of these inhomogeneities enables recovery toward the initial polarization state.

In summary, the present method demonstrates high sensitivity to polarization changes arising from refractive index modulations near USPL-induced filaments, thereby providing a robust means of characterizing such ultrafast laser–material interactions.

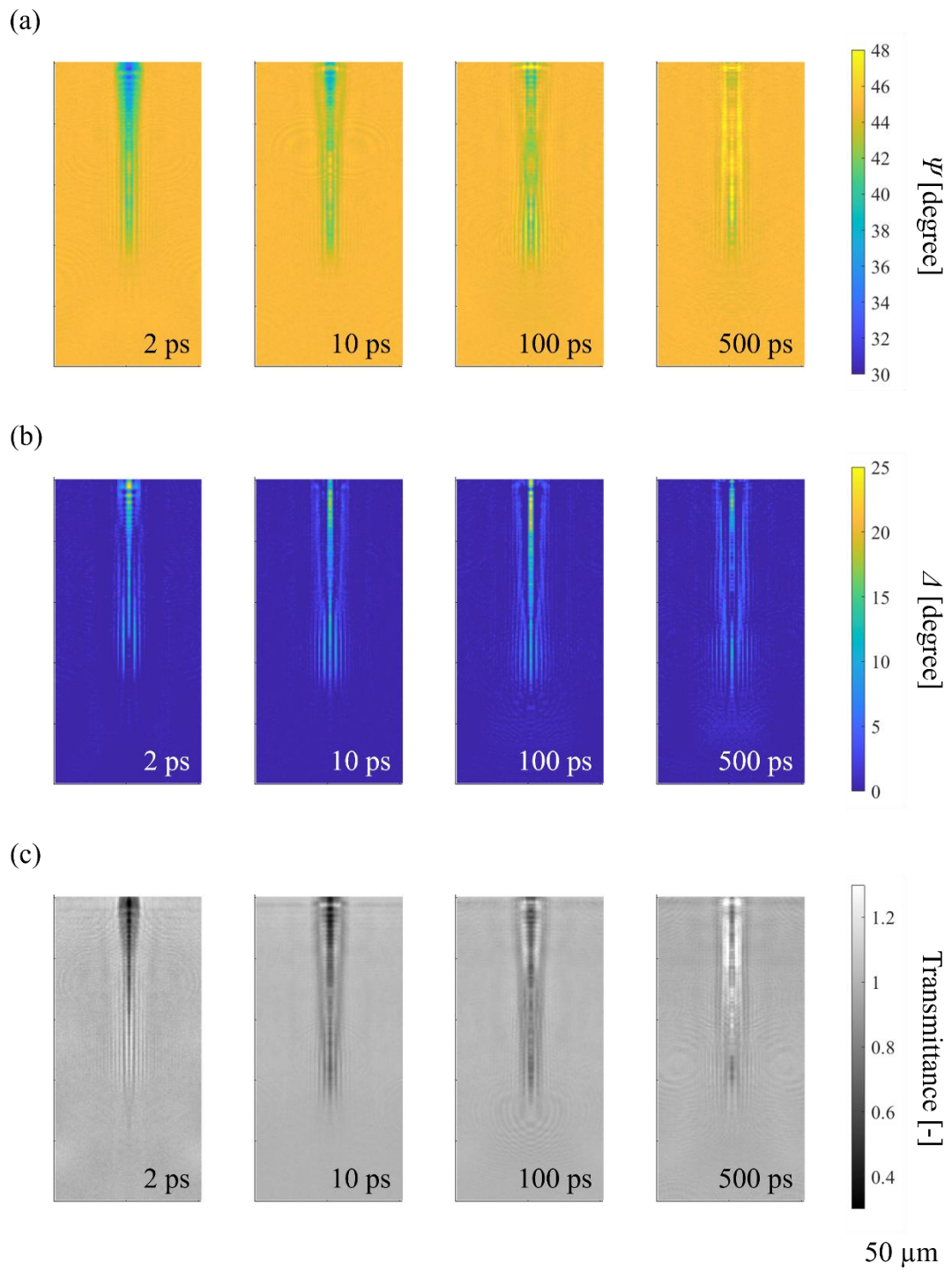


Fig. 4 Spatiotemporal evolution of polarization parameters and corresponding filaments. (a) Ψ [deg], (b) Δ [deg], and (c) transmittance [-].

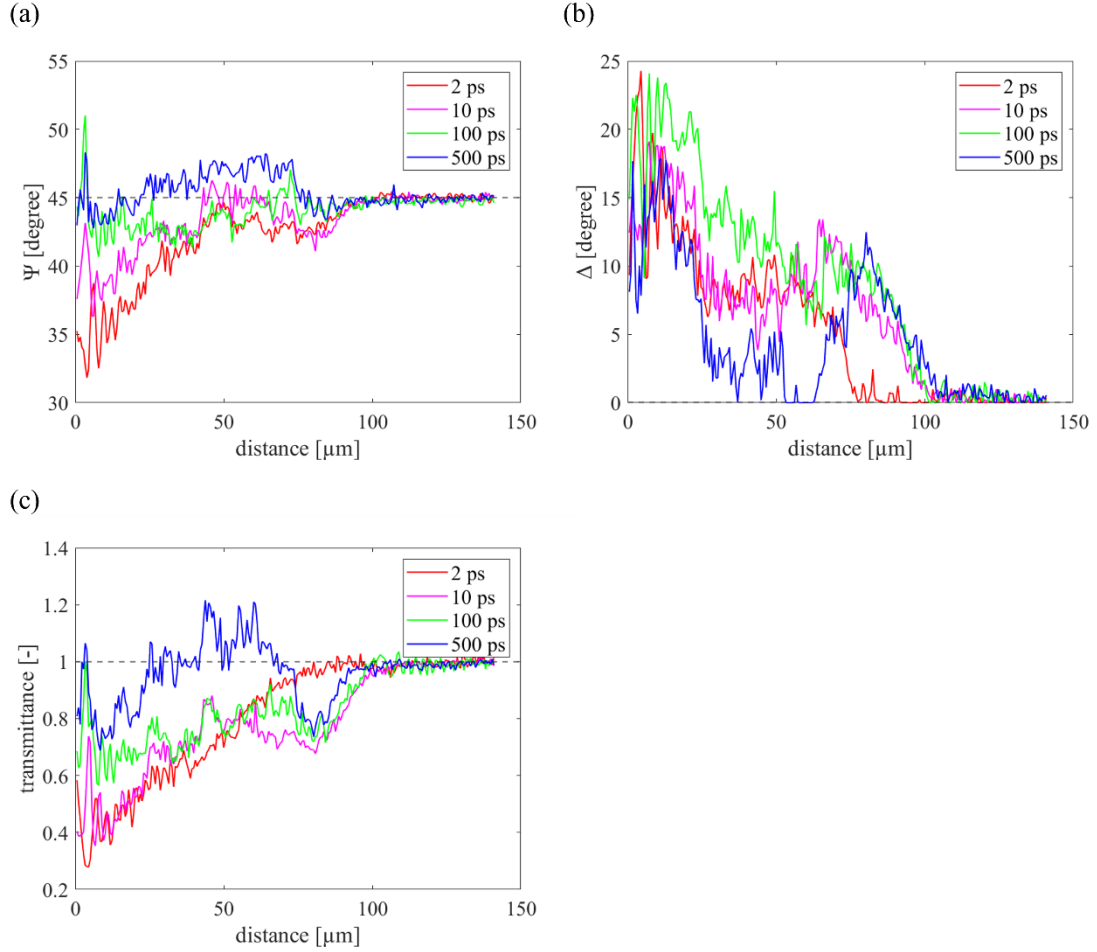


Fig. 5 Temporal evolution of polarization parameters and transmittance along the central axis of the filaments. (a) Ψ [deg], (b) Δ [deg], and (c) transmittance [-]. Plots are color-coded according to the elapsed time after USPL irradiation: red, magenta, green, and blue correspond to 2, 10, 100, and 500 ps, respectively.

Refractive Index Distribution in 2-ps USPL-Induced Filaments

Figure 6 shows the spatial distribution of the complex refractive index of the filament obtained using the proposed method. The regions where the refractive index deviates from that of pristine fused silica ($n_0 = 1.461$) correspond to the locations where the filament was induced (see Fig. 4(c)).

In general, the magnitude of the refractive index deviation from n_0 is closely related to the density of photoexcited electrons within the material. Regions subjected to stronger laser fields, where more significant electron excitation occurs, tend to exhibit larger deviations. These regions are typically aligned along the central axis of the filament, and the radial profile of the refractive index change is expected to follow a Gaussian distribution, reflecting the spatial intensity profile of the incident laser field. Furthermore,

as time progresses, the excited electrons gradually relax, leading to a corresponding reduction in the refractive index deviation. The present experimental results show good qualitative agreement with these general characteristics.

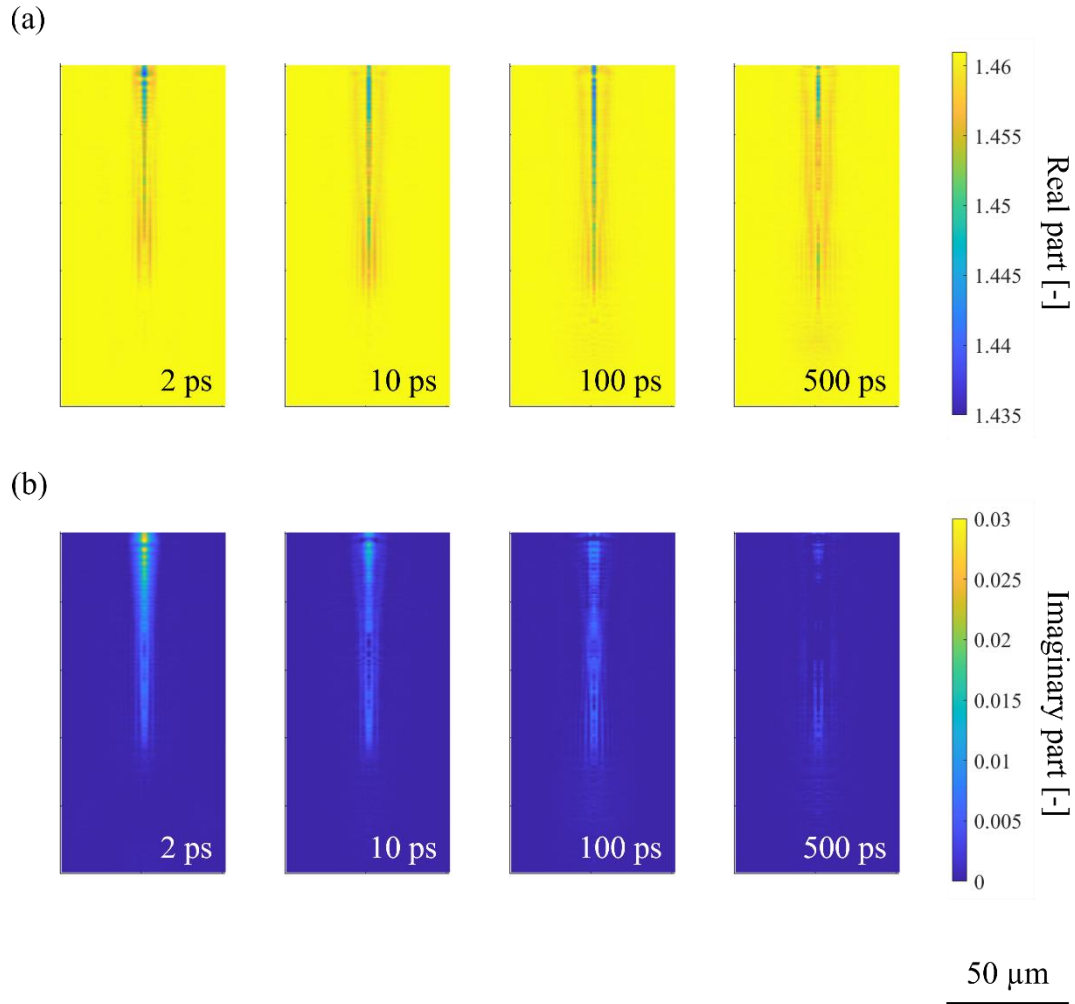


Fig. 6 Spatiotemporal evolution of the complex refractive index of the filament obtained using the proposed method. (a) real part [-], and (b) imaginary part [-].

Validation of the Proposed Method Through Comparative Analysis with Shadowgraphy

The reliability of the results obtained using the proposed method was assessed through a comparative analysis with both a conventional experimental technique and numerical simulations (for details, see Appendix 6 and 7, respectively). As a first step, the conventional method was employed to evaluate the imaginary component of the refractive index. Specifically, shadowgraphy was utilized, leveraging the established correlation between the transmittance of a probe beam and the material's absorption

coefficient. The outcomes derived from this approach are presented in Fig. 7(a). These results exhibit a strong qualitative consistency with those obtained via the proposed method (Fig. 6(b)). In both cases, the deviation of the refractive index from n_0 was spatially localized along the filament axis, with radial profiles exhibiting Gaussian-like attenuation. Furthermore, the temporal evolution of the measured signals was in accordance with the generally accepted relaxation dynamics of photoexcited electrons in the materials, which is likewise consistent with the results obtained by the proposed method. These findings provide indirect but compelling evidence supporting the reliability of the proposed method.

To enable a quantitative comparison, Fig. 7(b) illustrates the axial profiles obtained using both the proposed technique and shadowgraphy. For each delay time following USPL irradiation, data acquired by both methods are superimposed, with the proposed method denoted by red plots and shadowgraphy by blue plots. The comparison reveals a high degree of quantitative agreement between the two approaches. For instance, at a delay time of 2 ps, both methods yield values predominantly ranging from approximately 0.025 to 0.020 over a propagation distance of 0–25 μm . Furthermore, both profiles exhibit a similar asymptotic decay toward zero with nearly identical curvature, as shown in Fig. 7(b1). This level of agreement persists consistently across all subsequent delay times, as illustrated in Figs. 7(b2)–(b4). These results indicate that the measurements obtained via the proposed method are in excellent quantitative agreement with those derived from the conventional technique under all tested conditions. Consequently, the accuracy of the proposed method in evaluating the imaginary part is considered comparable to, or potentially superior to, that of established measurement techniques (see Appendix. 6 for a more comprehensive discussion).

Numerical Validation Based on the Drude Model

To further evaluate the reliability of the proposed method, numerical simulations were conducted. In these simulations, the real part of the refractive index corresponding to the experimentally obtained imaginary part was estimated computationally and compared with the measured values. This approach is justified by the established relationship between the real and imaginary components of the refractive index, which can be reasonably inferred using a classical model describing excited electrons in dielectrics (the Drude model). As detailed in Appendix. 7, this relationship is governed by the electron collision frequency ν , a parameter characterizing the dynamics of excited carriers. Reported values of ν typically lie in the range of 1×10^{15} to $1 \times 10^{16} \text{ s}^{-1}$ [19–24], thereby constraining the plausible values of the real part. Consequently, good agreement between

the computed and measured real parts, using a ν value within this reported range, may be regarded as indirect evidence supporting the validity of the proposed method.

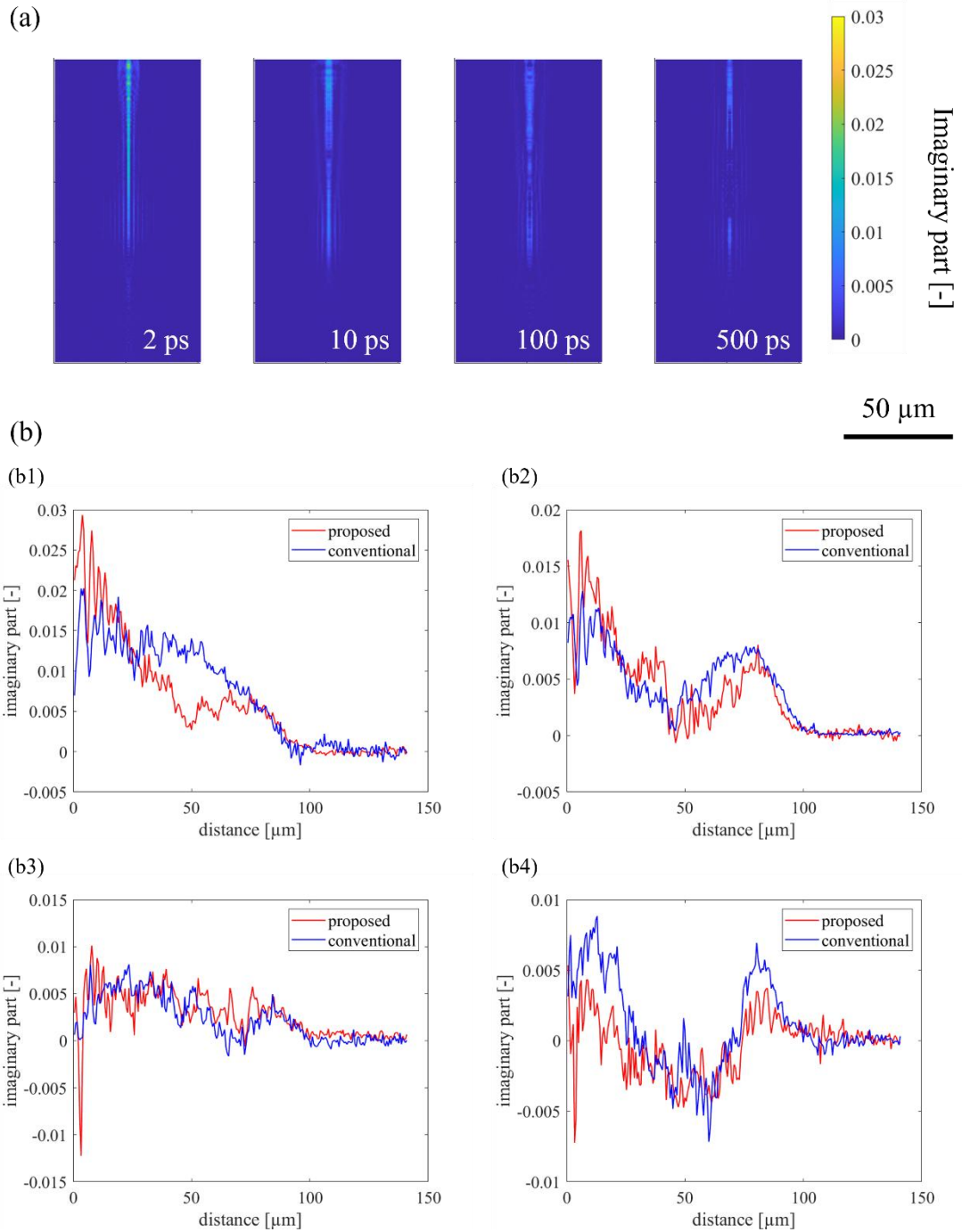


Fig. 7. Validation of the proposed measurement method using shadowgraphy. (a) Spatiotemporal evolution of the imaginary part measured by shadowgraphy. (b) Comparison of the measured results along the central axis of the filament; red plots represent the results obtained by the proposed method, while blue plots indicate those obtained by shadowgraphy.

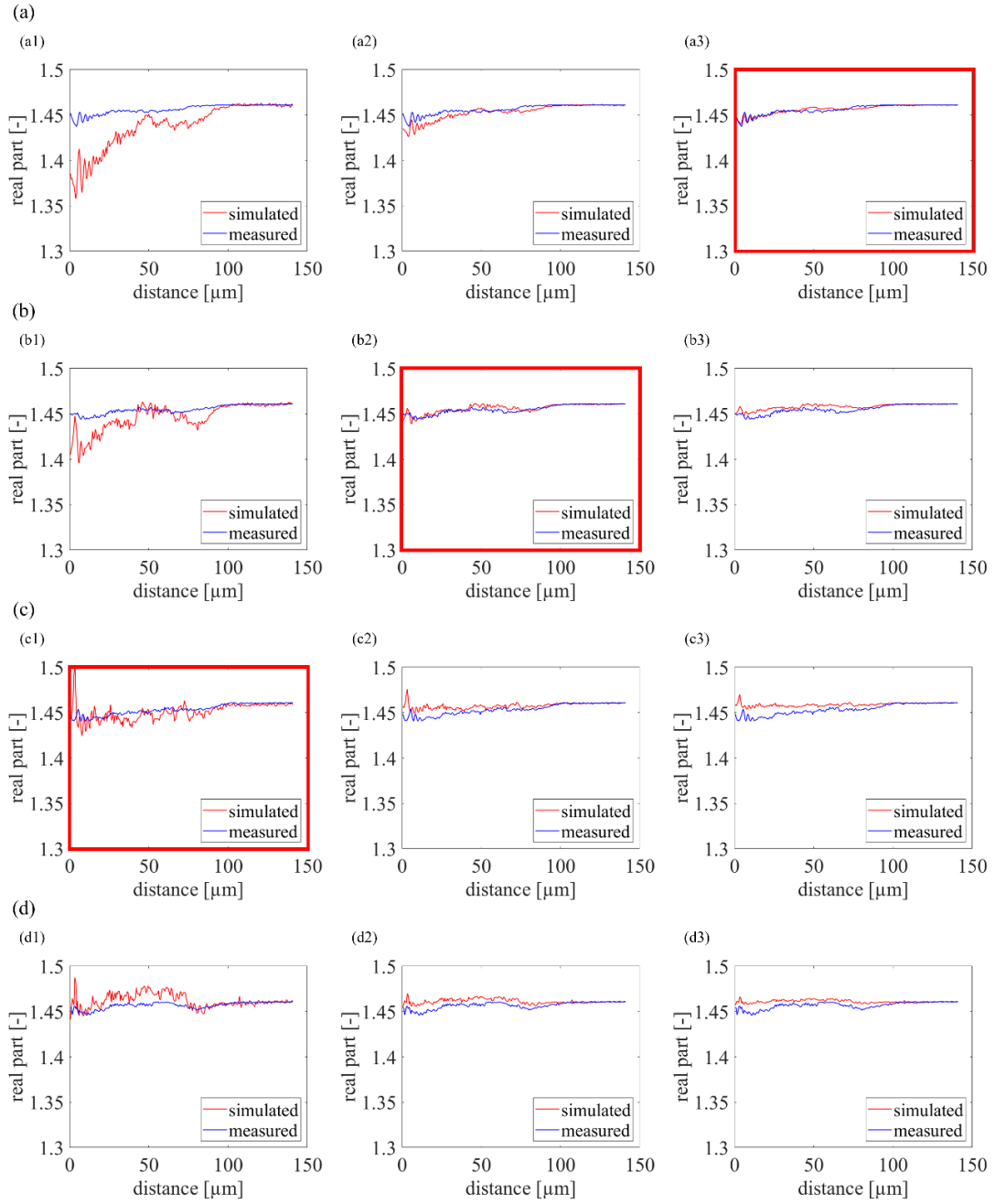


Fig. 8. Validation of the proposed measurement method through comparison with simulation results. Blue plots represent the results obtained using the proposed method, while red plots indicate corresponding simulation results. Panels (a)-(d) shows the results at delay times of 2, 10, 100, and 500 ps, respectively. Each panel comprises three subpanels, labeled (x1), (x2), and (x3), which present simulation results obtained with electron collision frequencies of $\nu = 1 \times 10^{15}$, 3×10^{15} , and $5 \times 10^{15} \text{ s}^{-1}$, respectively. The subpanel showing the closest agreement between the experimental and simulated results is enclosed by a red frame.

Figure 8 presents the results of the numerical simulations. Panels (a)–(d) show overlays of the experimentally measured values (blue curves) and the corresponding numerical estimates (red curves), both obtained at delay times ranging from 2 to 500 ps following USPL irradiation. In the simulations, the electron collision frequency ν was varied across three representative values: 1×10^{15} , 3×10^{15} , and $5 \times 10^{15} \text{ s}^{-1}$.

In the temporal range up to 100 ps post-irradiation (Figs. 8(a)–(c)), the simulations exhibit good agreement with the experimental data under all tested conditions. Specifically, the best match at 2 ps was obtained with $\nu = 5 \times 10^{15} \text{ s}^{-1}$ (Fig. 8(a3)); at 10 ps, with $\nu = 3 \times 10^{15} \text{ s}^{-1}$ (Fig. 8(b2)); and at 100 ps, with $\nu = 1 \times 10^{15} \text{ s}^{-1}$ (Fig. 8(c1)). Notably, the collision frequency ν yielding the best agreement between experimental and numerical results decreases with increasing delay time. This trend is physically consistent with the generally understood relaxation dynamics of excited electrons: the collision frequency ν reflects the rate of interactions between excited electrons and other carriers or phonons, and is typically higher during the early stages of excitation when electronic activity is most intense [19–24]. Accordingly, the observed temporal decrease in ν can be interpreted as indicative of progressive electron relaxation and a corresponding reduction in their kinetic energy.

In contrast, at a delay of 500 ps (Fig. 8(d)), a marked discrepancy emerges between the simulations and experimental results. A plausible explanation for this deviation is that, at this stage, the material state exceeds the validity range of the Drude model. Indeed, optical luminescence—phenomena not observed at earlier times—was detected near the filament under these conditions (Figs. 4(c) and 5(c)), suggesting the involvement of additional processes such as plasma luminescence that lie beyond the descriptive scope of the Drude model. Accordingly, the disagreement observed at this later time is attributed to the limitations of the underlying model, rather than a flaw in the proposed method itself. Nevertheless, a more comprehensive understanding of the phenomena occurring at this time scale will require further investigation.

Discussion

This study presents a novel method for spatiotemporally resolving the complex refractive index alterations induced by USPL irradiation in transparent dielectrics. While USPLs are known to generate transient, filamentary structures characterized by localized changes in material properties, the precise measurement of these dynamics—particularly of the complex refractive index—has remained challenging due to the limitations of existing diagnostic techniques. To address this, the authors developed a polarization-based imaging technique that analyzes the transmitted probe beam’s polarization state to extract

the full complex refractive index distribution in three dimensions with femtosecond temporal resolution. Notably, the proposed method enabled simultaneous detection of both the real and imaginary components of the refractive index—overcoming a major limitation of conventional techniques such as interferometry and shadowgraphy, which typically isolate only one component. The method successfully captured the evolution of refractive index variations in fused silica, revealing a strong correlation between refractive index modulation and the expected temporal relaxation behavior. The accuracy of the results was validated through quantitative comparisons with conventional shadowgraphy and further supported by numerical simulations based on the Drude model. Good agreement was observed across a range of delay times up to 100 ps, with the electron collision frequency decreasing over time in accordance with the expected relaxation dynamics of excited carriers. At longer timescales (>500 ps), deviations from simulation results were attributed to the breakdown of the Drude model, possibly due to emerging plasma luminescence, suggesting a complex regime warranting further investigation.

In conclusion, this work introduces a robust and generalizable technique for visualizing and quantifying ultrafast light - matter interactions, with significant implications for optimizing USPL-based micro/nanofabrication and advancing the understanding of nonequilibrium processes in dielectric media.

Acknowledgements

We would like to express our gratitude to the Japan Society for the Promotion of Science (24KJ0748), JST PRESTO (JPMJPR22Q1), and MEXT Q-LEAP (JPMXS0118067246).

Author contributions

Conceptualization: T.K. Methodology: T.K. Investigation: T.K. Visualization: T.K. Funding acquisition: N.S., Y.I., and T.K. Supervision: N.S. and Y.I. Writing—original draft: T.K. Writing—review and editing: T.K and Y.I.

Conflict of interest

The authors have no conflicts to disclose.

Data availability

Data underlying the results presented in this paper are not publicly available at this time but may be obtained from the authors upon reasonable request.

Reference

1. L. Wang, Y. Zhao, Y. Zhao, Y. Yang, T. Gong, L. Hao, T. Gong, and W. Ren. "Design and fabrication of bulk micromachined 4H-SiC piezoresistive pressure chips based on femtosecond laser technology." *Micromachines* **12**(1), 56 (2021). <https://doi.org/10.3390/mi12010056>.
2. K. Minoshima, A. M. Kowalevich, I. Hartl, E. P. Ippen, and J. G. Fujimoto. "Photonic device fabrication in glass by use of nonlinear materials processing with a femtosecond laser oscillator." *Optics Lett.* **26**(19), 1516-1518 (2001). <https://doi.org/10.1364/OL.26.001516>.
3. E. Thiénot, F. Domingo, E. Cambril, and C. Gosse. "Reactive ion etching of glass for biochip applications: Composition effects and surface damages." *Microelectron. Eng.* **83**(4-9), 1155-1158 (2006). <https://doi.org/10.1016/j.mee.2006.01.029>.
4. M. Malinauskas, A. Žukauskas, S. Hasegawa, Y. Hayasaki, V. Mizeikis, R. Buividas, and S. Juodkazis. "Ultrafast laser processing of materials: from science to industry." *Light: Science & Applications* **5**(8), e16133-e16133 (2016). <https://doi.org/10.1038/lsa.2016.133>.
5. R. R. Gattass and E. Mazur. "Femtosecond laser micromachining in transparent materials." *Nat. Photon.* **2**(4), 219-225 (2008). <https://doi.org/10.1038/nphoton.2008.47>.
6. A. Couairon and A. Mysyrowicz. "Femtosecond filamentation in transparent media." *Phys. Rep.* **441**(2-4), 47-189 (2007). <https://doi.org/10.1016/j.physrep.2006.12.005>.
7. G. Ren, Y. Ito, H. Sun, and N. Sugita. "Temporal-spatial characteristics of filament induced by a femtosecond laser pulse in transparent dielectrics." *Optics Exp.* **30**(4), 4954-4964 (2022). <https://doi.org/10.1364/OE.449874>.
8. X. Mao, S. S. Mao, and R. E. Russo. "Imaging femtosecond laser-induced electronic excitation in glass." *Appl. Phys. Lett.* **82**(5), 697-699 (2003). <https://doi.org/10.1063/1.1541947>.
9. F. Huang, J. Si, T. Chen, T. Shen, M. Shi, and X. Hou. "Temporal-spatial dynamics of electronic plasma in femtosecond laser induced damage." *Optics Exp.* **29**(10), 14658-14667 (2021). <https://doi.org/10.1364/OE.422346>.
10. K. Ishikawa, H. Kumagai, and K. Midorikawa. "High-power regime of femtosecond-laser pulse propagation in silica: Multiple-cone formation." *Phys. Rev. E* **66**(5), 056608 (2002). <https://doi.org/10.1103/PhysRevE.66.056608>
11. G. Ren, Y. Ito, R. Yoshizaki, H. Sun, J. Hattori, and N. Sugita, "Ultrafast dynamics and internal processing mechanism of silica glass under double-pulse femtosecond laser irradiation." *Opt. Express* **32**(18), 32408–32420 (2024). <https://doi.org/10.1364/OE.530465>
12. K. Bergner, B. Seyfarth, K. A. Lammers, T. Ullsperger, S. Döring, M. Heinrich, M. Kumkar, D. Flamm, A. Tünnermann, and S. Nolte. "Spatio-temporal analysis of glass volume processing using ultrashort laser pulses." *Appl. Optics* **57**(16), 4618-4632 (2018).

<https://doi.org/10.1364/AO.57.004618>.

13. T. Pflug, M. Olbrich, and A. Horn. "Electron dynamics in fused silica after strong field laser excitation detected by spectroscopic imaging pump-probe ellipsometry." *Phys. Rev. B* **106**(1), 014307 (2022). <https://doi.org/10.1103/PhysRevB.106.014307>
14. H. Fujiwara. "Spectroscopic ellipsometry: Principles and applications." John Wiley and Sons (2009).
15. M. Wakagi, H. Fujiwara, and R. W. Collins, "Real time spectroscopic ellipsometry for characterization of the crystallization of amorphous silicon by thermal annealing." *Thin Solid Films* **313**, 464-468 (1998). [https://doi.org/10.1016/S0040-6090\(97\)00865-1](https://doi.org/10.1016/S0040-6090(97)00865-1)
16. J. Lee, P. I. Rovira, I. An, and R. W. Collins, "Alignment and calibration of the MgF₂ biplate compensator for applications in rotating-compensator multichannel ellipsometry." *J. Opt. Soc. Am. A* **18**(8), 1980-1985 (2001). <https://doi.org/10.1364/JOSAA.18.001980>
17. P. S. Hauge, "Generalized rotating-compensator ellipsometry." *Surf. Sci.* **56** 148-160 (1976). [https://doi.org/10.1016/0039-6028\(76\)90442-8](https://doi.org/10.1016/0039-6028(76)90442-8)
18. J. Lee, P. I. Rovira, I. An, and R. W. Collins, "Rotating-compensator multichannel ellipsometry: Applications for real time Stokes vector spectroscopy of thin film growth. " *Rev. Sci. Instrum.*, **69**(4), 1800-1810 (1998). <https://doi.org/10.1063/1.1148844>
19. C. Sarpe, J. Köhler, T. Winkler, M. Wollenhaupt, and T. Baumert. "Real-time observation of transient electron density in water irradiated with tailored femtosecond laser pulses." *New J. Phys.* **14**(7), 075021 (2012). <https://doi.org/10.1088/1367-2630/14/7/075021>.
20. S. Guizard, A. Semerok, J. Gaudin, M. Hashida, P. Martin, and F. Quéré. "Femtosecond laser ablation of transparent dielectrics: measurement and modelisation of crater profiles." *Appl. Surface Sci.* **186**(1-4), 364-368 (2002). [https://doi.org/10.1016/S0169-4332\(01\)00681-X](https://doi.org/10.1016/S0169-4332(01)00681-X).
21. F. Quéré, S. Guizard, and P. Martin. "Time-resolved study of laser-induced breakdown in dielectrics." *Europhys. Lett.* **56**(1) (2001). <https://doi.org/10.1209/epl/i2001-00499-9>.
22. B. Rethfeld, H. Krutsch, and D. H. H. Hoffmann. "Tracing Laser - Induced Dielectric Breakdown in Solids." *Contribut. Plasma Phys.* **50**(1), 16-20 (2010). <https://doi.org/10.1002/ctpp.201010005>.
23. B. Rethfeld, O. Brenk, N. Medvedev, H. Krutsch, and D. H. H. Hoffmann. "Interaction of dielectrics with femtosecond laser pulses: application of kinetic approach and multiple rate equation." *Appl. Phys. A* **101**, 19-25 (2010). <https://doi.org/10.1007/s00339-010-5780-3>.
24. M. D. Feit, A. M. Komashko, and A. M. Rubenchik. "Ultra-short pulse laser interaction with transparent dielectrics." *Appl. Phys. A* **79** (2004). <https://doi.org/10.1007/s00339-004-2683-1>.

Supplementary Material for

Time-resolved and three-dimensional elucidation of the complex refractive index alteration induced by ultrashort laser pulses

Takumi Koike^{1*}, Yusuke Ito¹, Naohiko Sugita¹

¹*Department of Mechanical Engineering, School of Engineering, The University of Tokyo, 7-3-1 Hongo, Bunkyo, Tokyo 113-8656, Japan*

* Corresponding author: t.koike@mfg.t.u-tokyo.ac.jp (Takumi Koike)

1. Details on Data Processing Methodology

With a fixed optical delay between the processing and observation pulses, the angle of the polarizer in the setup was systematically varied in 20° increments from 0° to 180° , resulting in ten distinct measurement conditions (see the left diagram in Fig. 2). For each polarizer angle condition, two types of images were acquired: one taken without USPL irradiation (BG images), and the other captured during filament induction (filament images). Image acquisition was performed on three separate occasions, yielding three pairs of filament and corresponding BG images for each condition. All images were saved in raster format, where each pixel holds a real-valued intensity corresponding to the detected light at that position, with higher values indicating stronger intensity. The following preprocessing steps were applied to these data:

- I. Each filament image was normalized by dividing its pixel values by those of the corresponding BG image, resulting in intensity ratios typically ranging from 0 to 1.
- II. The normalized image was then multiplied by the average pixel value of the corresponding BG image. This correction step mitigates fluctuations in overall light intensity arising from factors unrelated to material properties, such as variations in the laser amplifier or imaging system.
- III. The corrected images obtained under each polarizer angle condition were averaged across the three measurement sessions to reduce inter-experimental variability.
- IV. Assuming axial symmetry of the refractive index distribution, symmetric images were generated by averaging pixel values across both sides of the filament axis. In subsequent analyses, only the axisymmetric half of the image was retained.

Through these procedures, the light intensity distribution as a function of polarizer angle, denoted $I(\alpha)$, was obtained for each condition (see the right diagram in Fig. 2).

2. Jones Calculus-Based Derivation of Eq. (1)

In this section, the derivation of Eq. (1) is presented based on Jones calculus, the fundamentals of which are described in Ref. [14]. For clarity and conciseness, the notations summarized in Table A1 are employed throughout this derivation. Using these abbreviations, Eq. (1) can be rewritten as:

$$\mathbf{E}(\alpha) \propto \mathbf{P}_y \mathbf{M}_R(\alpha + \theta) \mathbf{S} \mathbf{J}_{in} \quad (\text{A1})$$

Table A1 Abbreviations and corresponding Jones matrices/vectors.

Optical elements	Abbreviations	Jones matrix/vector
Polarizer	\mathbf{P}_y	$\begin{bmatrix} 0 & 0 \\ 0 & 1 \end{bmatrix}$
Rotation matrix	$\mathbf{M}_R(\varphi)$	$\begin{bmatrix} \cos \varphi & \sin \varphi \\ -\sin \varphi & \cos \varphi \end{bmatrix}$
Transmission of material	\mathbf{S}	$\begin{bmatrix} \sin \Psi \exp(-j\Delta) & 0 \\ 0 & \cos \Psi \end{bmatrix}$
Incident electric field	\mathbf{J}_{in}	$\begin{bmatrix} \sin \psi \exp(-j\delta) \\ \cos \psi \end{bmatrix}$

Multiplication of the incident Jones vector \mathbf{J}_{in} by the matrix \mathbf{S} from the left yields the polarization state after transmission through the material. This follows from the relationship between the transmittance ratio of the P- and S-polarized components t_p/t_s , and the ellipsometric parameters Ψ and Δ :

$$\tan \Psi \exp(-j\Delta) \equiv \frac{t_p}{t_s} = \frac{E'_P/E_P}{E'_S/E_S} \Rightarrow \frac{E'_P}{E'_S} = \tan \Psi \exp(-j\Delta) \frac{E_P}{E_S} \quad (\text{A2})$$

Thus, the transmitted electric field vector can be written as:

$$\therefore \begin{bmatrix} E'_P \\ E'_S \end{bmatrix} \propto \begin{bmatrix} \sin \Psi \exp(-j\Delta) & 0 \\ 0 & \cos \Psi \end{bmatrix} \begin{bmatrix} E_P \\ E_S \end{bmatrix} = \mathbf{S} \mathbf{J}_{in} \quad (\text{A3})$$

Here, $E_{P/S}$ and $E'_{P/S}$ denote the electric field amplitudes for the P/S components before and after transmission, respectively.

Subsequent multiplication by the rotation matrix $\mathbf{M}_R(\alpha+\theta)$ and the polarizer matrix \mathbf{P}_y in this order yields the electric field after passing through the analyzer, whose transmission axis is tilted by an angle $\alpha+\theta$ from the vertical. This process is illustrated schematically in Fig. A1. Specifically, $\mathbf{M}_R(\alpha+\theta)$ represents a counterclockwise rotation of

the coordinate system by $\alpha+\theta$ (Fig. A1(b)), and P_y corresponds to a polarizer whose transmission axis is aligned with the new y' -axis (Fig. A1(c)).

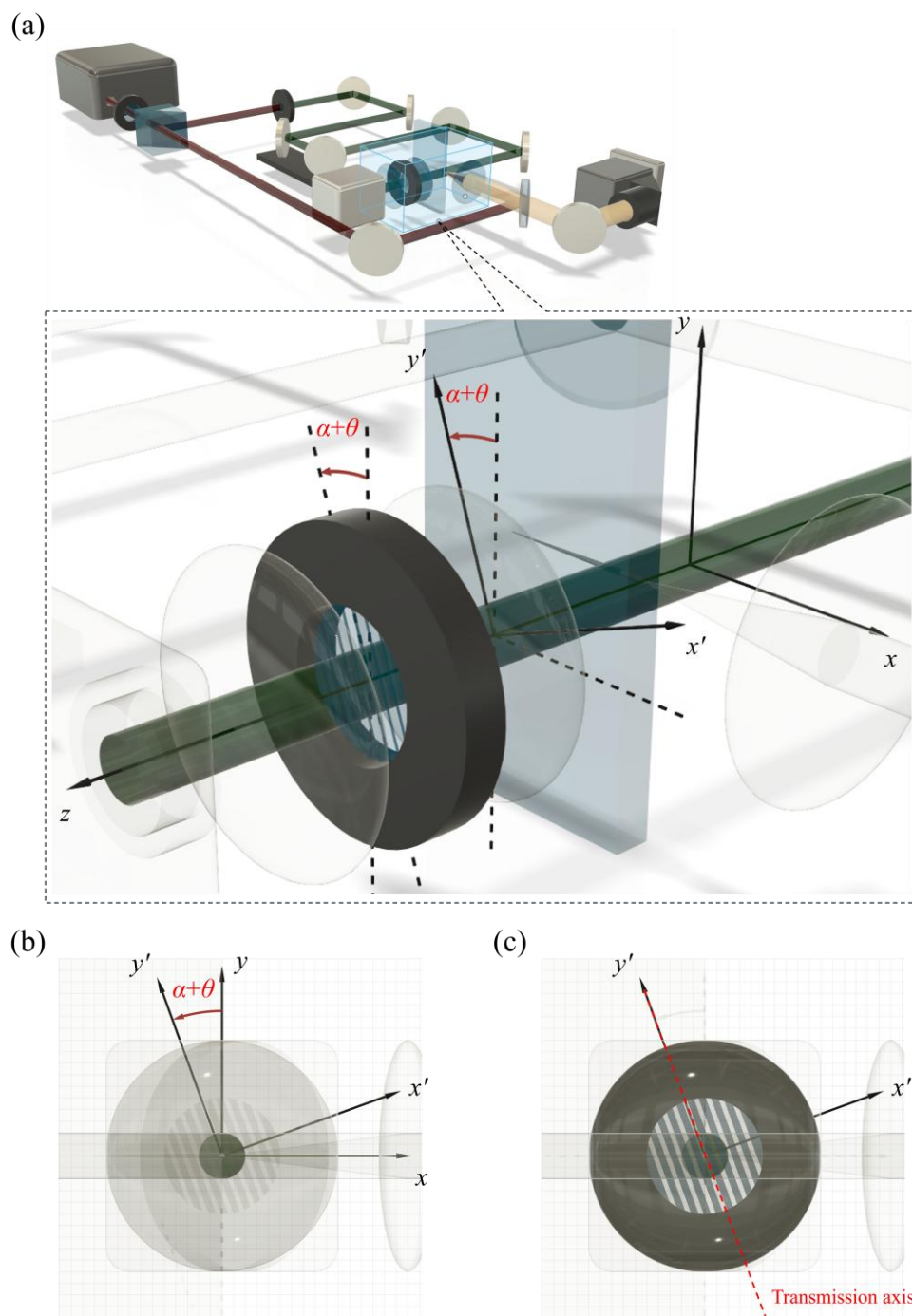


Fig. A1 Schematic representation of the Jones matrix-based modeling of light transmission and analysis. (a) Overall optical setup corresponding to Eq. (A1); (b) Definition of the rotated coordinate system by angle $\alpha+\theta$; (c) Orientation of the polarizer along the y' -axis.

3. Estimation Procedure for the Polarization Parameters Ψ and Δ

The polarization parameters Ψ and Δ were estimated by identifying the theoretical expression $I(\alpha)$ that best fits the experimentally measured light intensity $I'(\alpha)$, using the least-squares approximation method. This estimation process involves multiple steps, as several additional parameters—the initial orientation angle of the polarizer θ and the initial polarization parameters of the observation pulse ψ and δ —must also be determined. The following subsections provide a detailed description of each step involved in this estimation procedure.

3-1. Determination of the Initial Orientation Angle θ

The orientation angle θ of the polarizer cannot be known a priori due to the mechanical ambiguity introduced by the engagement of threaded components in the polarizer assembly, specifically between the mounted wire-grid polarizer (WP25M-UB1, Thorlabs) and the continuous rotation mount (RSP1D/M, Thorlabs). To determine θ , the experimentally measured intensity $I'(\alpha)$ for an S-polarized pulse—whose polarization state is known in advance—was compared with the theoretical intensity $I(\alpha)$, which is given by Eq. (A5). The value of θ was obtained by minimizing the least-squares error between $I'(\alpha)$ and $I(\alpha)$.

$$\begin{aligned} \mathbf{E}'(\alpha) &\propto \begin{bmatrix} 0 & 0 \\ 0 & 1 \end{bmatrix} \begin{bmatrix} \cos(\alpha + \theta) & \sin(\alpha + \theta) \\ -\sin(\alpha + \theta) & \cos(\alpha + \theta) \end{bmatrix} \begin{bmatrix} 0 \\ 1 \end{bmatrix} \\ &= \begin{bmatrix} 0 \\ \cos(\alpha + \theta) \end{bmatrix} \end{aligned} \quad (\text{A4})$$

$$\begin{aligned} I'(\alpha) &= A' |\mathbf{E}'(\alpha)|^2 \\ &= A' \cos^2(\alpha + \theta) \end{aligned} \quad (\text{A5})$$

Here, the measured intensity $I'(\alpha)$ was spatially averaged over the entire imaging region, based on the assumption that light propagating in free space ideally exhibits a uniform intensity distribution. The spatial fluctuations in the measured data were therefore treated as noise and excluded from the estimation of θ . The value of θ obtained in this step was subsequently applied in all following estimations.

3-2. Estimation of the Initial Polarization Parameters ψ and δ

The initial polarization parameters ψ and δ were introduced to account for changes induced by second-harmonic generation (SHG) in the nonlinear optical crystal. Since the polarization state after SHG varies depending on the crystal properties, these parameters cannot be assumed a priori. To estimate these values, the experimentally measured

intensity $I''(\alpha)$ was compared with its theoretical expression $I''(\alpha)$. The optimal parameters were again obtained by minimizing the least-squares error.

$$\begin{aligned} \mathbf{E}''(\alpha) & \propto \begin{bmatrix} 0 & 0 \\ 0 & 1 \end{bmatrix} \begin{bmatrix} \cos(\alpha + \theta) & \sin(\alpha + \theta) \\ -\sin(\alpha + \theta) & \cos(\alpha + \theta) \end{bmatrix} \begin{bmatrix} \sin \psi \exp(-j\delta) \\ \cos \psi \end{bmatrix} \\ & = \begin{bmatrix} 0 \\ -\sin \psi \exp(-j\delta) \sin(\alpha + \theta) + \cos \psi \cos(\alpha + \theta) \end{bmatrix} \end{aligned} \quad (\text{A6})$$

$$\begin{aligned} I''(\alpha) & = A'' |\mathbf{E}''(\alpha)|^2 \\ & = A'' |-\sin \psi \exp(-j\delta) \sin(\alpha + \theta) + \cos \psi \cos(\alpha + \theta)|^2 \end{aligned} \quad (\text{A7})$$

The waveform $I''(\alpha)$ may appear nearly flat either when the amplitude A'' is small or when specific values of ψ and δ lead to destructive interference (see Fig. A2). To remove this ambiguity, the mean intensity over all polarizer angles was evaluated, leading to the relation:

$$\begin{aligned} & \frac{1}{\pi} \int_0^\pi A'' |-\sin \psi \exp(-j\delta) \sin(\alpha + \theta) + \cos \psi \cos(\alpha + \theta)|^2 d\alpha \\ & = \frac{A''}{2} \end{aligned} \quad (\text{A8})$$

This allows A'' to be determined independently from the mean of $I''(\alpha)$, enabling unique estimation of ψ and δ through least-squares fitting.

In practice, this estimation can be integrated with the procedure described in Section 3-3. Specifically, the measured intensity $I''(\alpha)$ may be replaced by the spatially averaged intensity over regions sufficiently distant from the filament, where the polarization state after SHG is assumed to remain unaltered. This assumption is justified by the experimental geometry: the probe light enters perpendicularly to the side surface of the sample, such that polarization modifications other than SHG are expected to be localized near the filament.

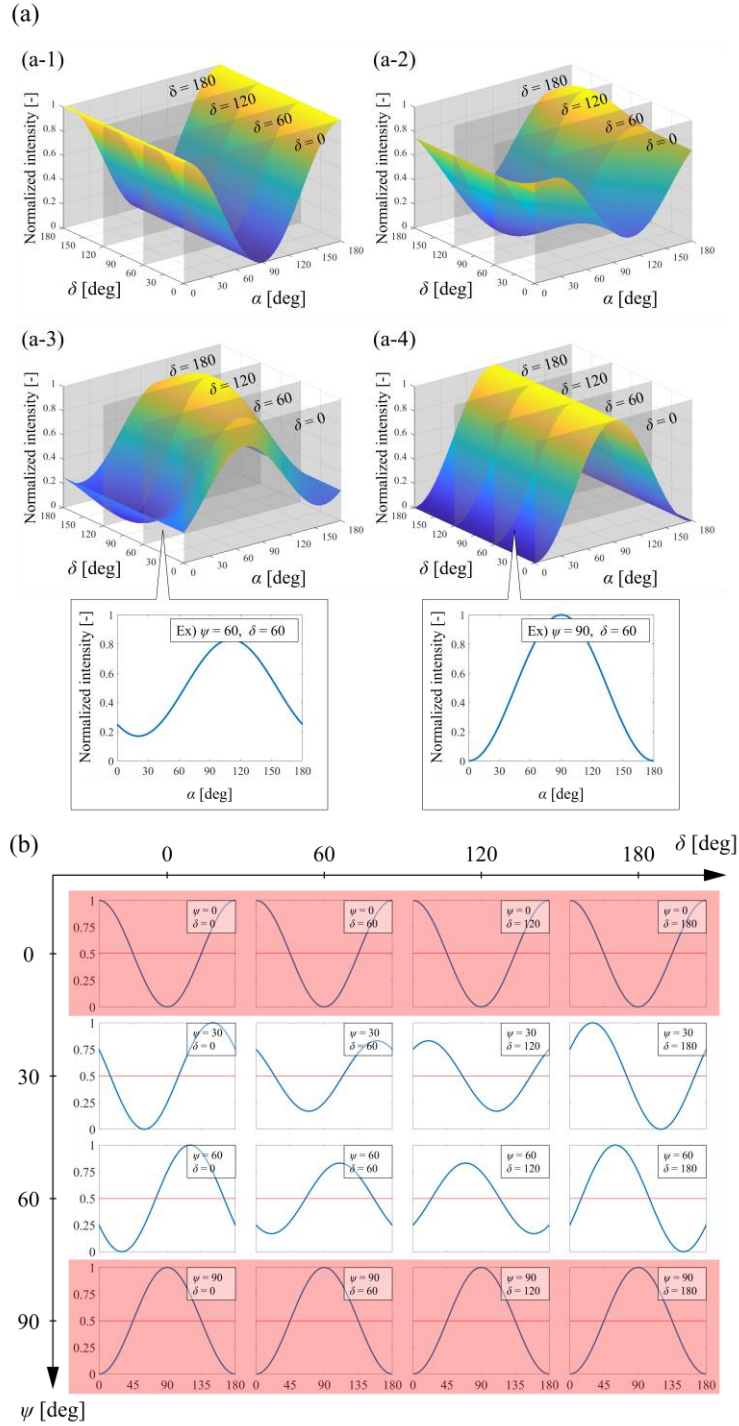


Fig. A2 Dependence of Normalized Theoretical Intensity $I''(\alpha)$ on Polarization Parameters ψ , δ , and α . (a) representative surface plots; (a-1)–(a-4) surface views for fixed $\psi = 0^\circ, 30^\circ, 60^\circ, 90^\circ$, varying δ and α ; (b) tiled cross-sectional profiles of $I''(\alpha)$ versus α for various combinations of ψ and δ . red-shaded regions in panel (b) indicate parameter domains with potential least-squares fitting instability, which are avoided in this study.

3-3. Estimation of Polarization Parameters Ψ and Δ

Finally, the previously determined parameters θ , ψ , and δ were used to estimate the polarization parameters of interest, Ψ and Δ , through least-squares fitting of the theoretical intensity waveform $I(\alpha)$ to the measured data $i(\alpha)$.

Fig. A3 presents the representative normalized waveforms as functions of Ψ and Δ . Unlike in the previous step, these waveforms do not exhibit distinctive features beyond the fact that their mean values are determined solely by Ψ . Consequently, the analytical strategy employed in Section 3-2 cannot be directly applied here. Nonetheless, the waveform can be characterized by three independent features—its mean intensity, the deviation of its extrema from the mean, and its phase offset—corresponding to three unknowns: the amplitude A , and the polarization parameters Ψ and Δ . Therefore, simultaneous determination of all three parameters is, in principle, feasible. While the same principle formally applies to the analysis in Section 3-2, it should be noted that the robustness of parameter estimation generally improves when the number of free parameters is minimized. For this reason, the amplitude A'' was preliminarily estimated prior to the determination of ψ and δ in Section 3-2.

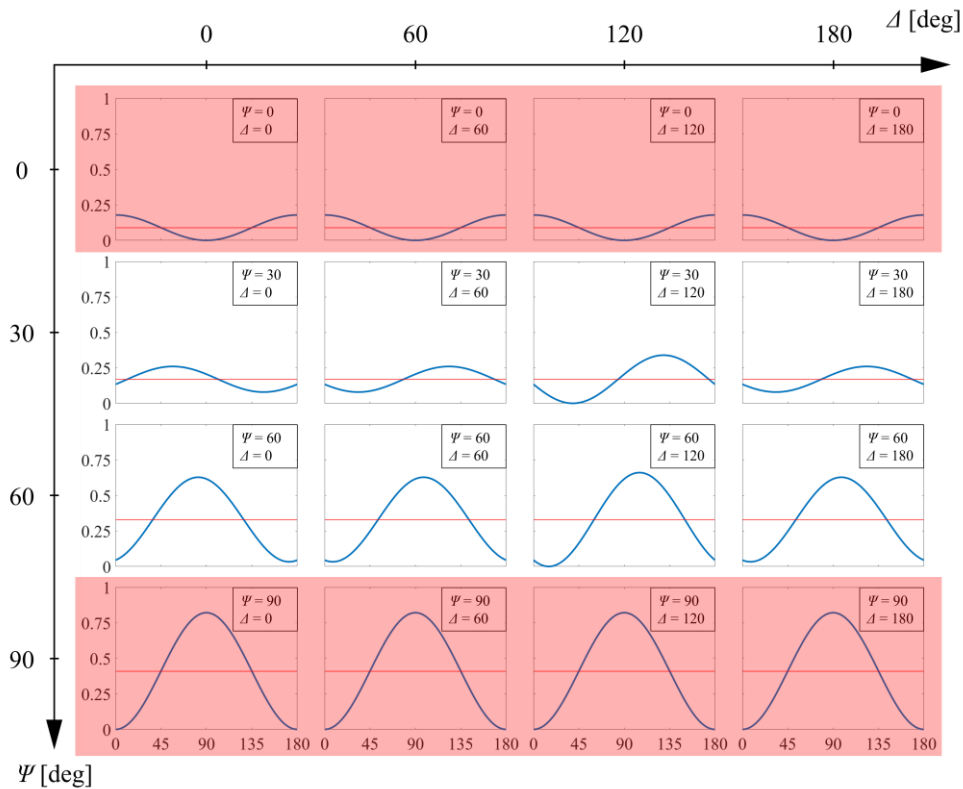


Fig. A3 Tiled Profiles of Normalized $I(\alpha)$ as Functions of Polarization Parameters Ψ and Δ , with red-shaded regions indicating potential least-squares fitting instability, which are avoided in this study.

4. Analysis of Fresnel Effects in Polarization

In the main text, birefringence was assumed to be the dominant mechanism underlying the observed variations in the polarization state of transmitted light. This supplementary section presents a quantitative evaluation to validate this assumption. As previously noted, additional contributions may arise from multiple reflections at interfaces between regions of differing refractive indices, as well as from Fresnel refractions at such boundaries. Among these, the effect of multiple reflections is generally negligible in absorbing media such as filaments [15]. Consequently, the present analysis is devoted to quantifying the influence of Fresnel effects.

To this end, an extended analytical framework was employed, incorporating both birefringence and Fresnel effects while maintaining the same optical configuration used in the main text (see Fig. A4). The resulting refractive index distribution obtained from this extended framework was then compared with that obtained using the birefringence-only model described in the main text. Hereafter in this appendix, results derived from the extended analysis are referred to as the *Fresnel-inclusive results*, whereas those obtained using the birefringence-only model are denoted as the *Reference results*. A close agreement between the two would indicate that Fresnel effects indeed play only a minor role in the observed polarization changes.

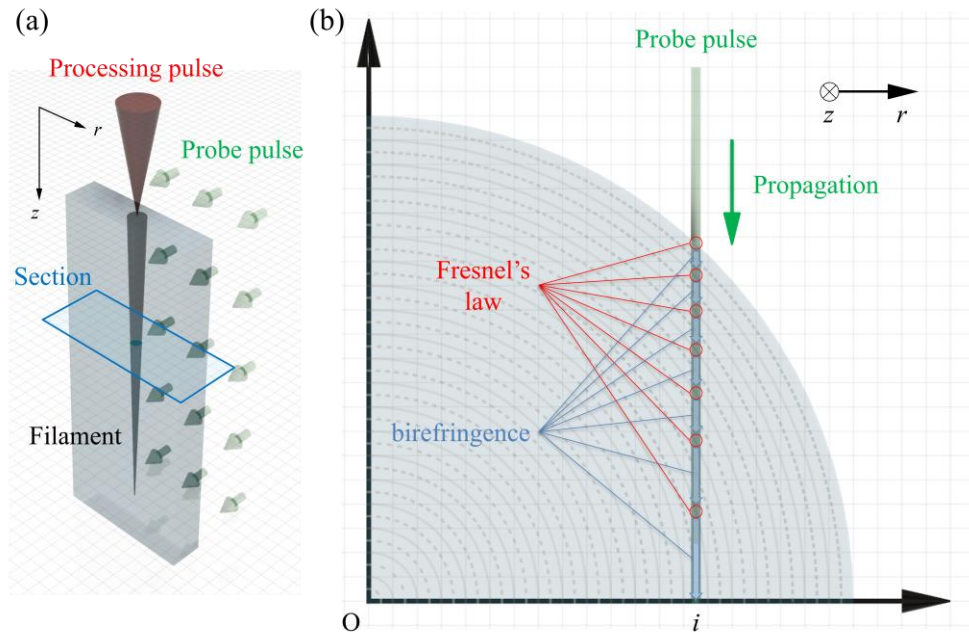


Fig. A4 Relationship between the USPL-induced filament and the polarization state change of the probe pulse. (a) Perspective view, (b) Cross-sectional view at $z = l$, incorporating both Fresnel effects and birefringence.

To quantitatively evaluate the contribution of Fresnel effects, we derived Eq. (A9), which describes the change in the transmission ratio and, accordingly (cf. Eq. (3)), the corresponding alteration in the polarization state. This formulation accounts for the interaction of an observation pulse with concentric refractive index layers from $r = k+1$ to $r = k$. The angles β and β' denote the incidence and refraction angles at the interface, respectively (see Fig. A5). δ_{Fresnel} signifies a minor alteration in the physical quantity induced by Fresnel effect. All other parameters and coordinates are defined in accordance with those adopted in the main text.

$$\begin{aligned} \delta_{\text{Fresnel}} \frac{t_p}{t_s} \Big|_{r=k \sim k+1}^{z=l} &= \delta_{\text{Fresnel}} \{ \tan \Psi \exp(-j\Delta) \} \Big|_{r=k \sim k+1}^{z=l} \\ &= \frac{N_{k+1}^l \cos \beta + N_k^l \cos \beta'}{N_k^l \cos \beta + N_{k+1}^l \cos \beta'}. \end{aligned} \quad (\text{A9})$$

Here, the angle β' in Eq. (A9) satisfies Snell's law:

$$N_k^l \sin \beta' = N_{k+1}^l \sin \beta \quad (\text{A10})$$

Meanwhile, the incident angle β is geometrically determined from triangle $\triangle OAB$ in Fig. A5, and is given by:

$$\beta = \sin^{-1} \left(\frac{i}{k + 0.5} \right) \quad (\text{A11})$$

Substituting Eqs. (A10) and (A11) into Eq. (A9) yields:

$$\begin{aligned} \delta_{\text{Fresnel}} \{ \tan \Psi \exp(-j\Delta) \} \Big|_{r=k \sim k+1}^{z=l} &= \frac{N_{k+1}^l \cos \left\{ \sin^{-1} \left(\frac{i}{k + 0.5} \right) \right\} + N_k^l \sqrt{1 - \left(\frac{N_{k+1}^l \frac{i}{k + 0.5}}{N_k^l} \right)^2}}{N_k^l \cos \left\{ \sin^{-1} \left(\frac{i}{k + 0.5} \right) \right\} + N_{k+1}^l \sqrt{1 - \left(\frac{N_{k+1}^l \frac{i}{k + 0.5}}{N_k^l} \right)^2}} \end{aligned} \quad (\text{A12})$$

The cumulative effect on the polarization state after propagation through all concentric layers—taking into account both birefringence and Fresnel effects—is expressed as a product of the individual contributions at each segment. This is given by combining Eq. (6) from the main text with Eq. (A12), where i_{max} denotes the terminal radial coordinate

within the imaging region:

$$\begin{aligned} & \tan \Psi \exp(-j\Delta)|_{r=i}^{z=l} \\ & = \prod_{k=i}^{i_{max}} \left[\delta \{ \tan \Psi \exp(-j\Delta) \} |_{r=k \sim k+1}^{z=l} \cdot \delta_{\text{Fresnel}} \{ \tan \Psi \exp(-j\Delta) \} |_{r=k \sim k+1}^{z=l} \right]^2 \end{aligned} \quad (\text{A13})$$

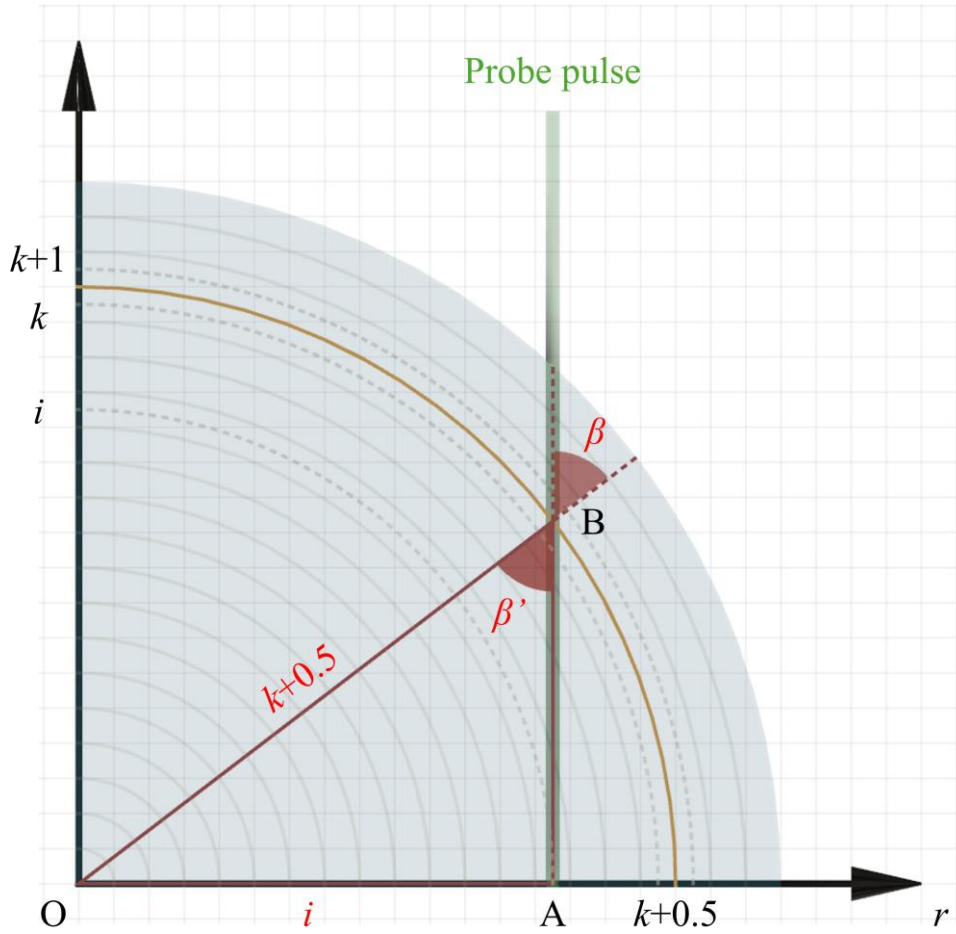


Fig. A5 Cross-Sectional Geometry of Filament with Relevant Parameters for Quantitative Fresnel Effect Evaluation.

Figure A6 presents the spatiotemporal distribution of Fresnel-inclusive results. Panels (a) and (b) show the real and imaginary components respectively. These results exhibit excellent consistency with the Reference results in both spatial and temporal dimensions (cf. Fig. 6), thereby supporting the assumption that Fresnel contributions are marginal.

To quantitatively assess the discrepancy between these results, the relative error was calculated. Specifically, the absolute difference between the two results at each condition was normalized by the absolute value of the corresponding Reference result, and the

outcome was expressed as a percentage. This approach enables a direct quantification of the Fresnel effect's contribution to polarization changes in relative terms. The resulting distribution is shown in panel (c). As evident from the figure, the relative error remains below $2.5 \times 10^{-4}\%$ across all conditions, with the maximum deviation reaching only $2.3683 \times 10^{-4}\%$. It is worth noting that the observed discrepancy is predominantly localized near the filament axis. This behavior is attributed, at least in part, to the numerical method employed in solving Eq. (A13). Unlike Eq. (A14), this equation cannot be linearized by any known transformation, rendering the numerical technique described in Appendix 5 inapplicable. In this analysis, the refractive index profile was determined sequentially from the outermost radial position toward the center. Consequently, numerical errors inherently accumulate as the calculation proceeds inward, leading to a concentration of error near the axis of symmetry. Therefore, if one accounts for this inevitable error accumulation inherent to the computational scheme, it can be inferred that the actual contribution of Fresnel effects is likely even smaller than indicated in Fig. A6(c). These findings further corroborate the assumption that Fresnel effects have a negligible impact on the polarization state under the present conditions, thereby affirming the validity of the analytical model described by Eq. (6).

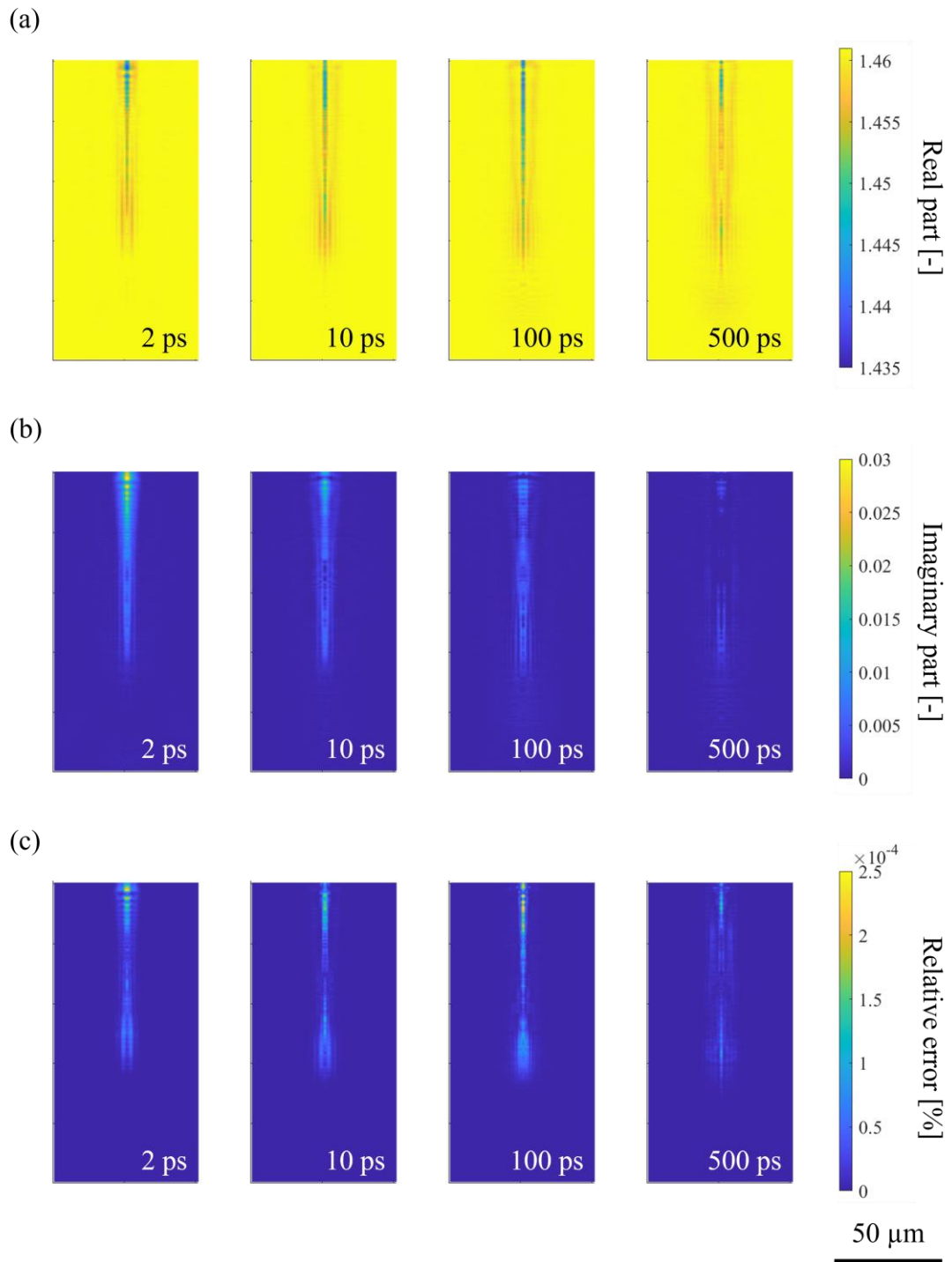


Fig. A6 Spatiotemporal Distribution of Fresnel-Inclusive Results and Relative Error Compared to Reference Results: (a) real part, (b) imaginary part of refractive index, and (c) relative error.

5. Solution of Eq. (6) Using Matrix Computation

Equation (6) is linearized by taking the natural logarithm of both sides, enabling its solution through standard linear algebraic techniques. This transformation allows the simultaneous reconstruction of the refractive index across all radial positions within a given cross-sectional plane at a fixed axial coordinate z , while also mitigating the accumulation of numerical errors toward the central axis.

Applying the natural logarithm to both sides of Eq. (6) yields the following expression. For notational simplicity, the coordinate designation $z = l$ is omitted in the subsequent discussion. Additionally, the notations $\rho_i \equiv \tan \Psi \exp(-j\Delta)|_{r=i}$ is adopted.

$$\begin{aligned} \rho_i &= \prod_{k=i}^{i_{max}} \left[\exp \left\{ \frac{2\pi d_k^i j}{\lambda} (N_k - N_{k+1}) \right\} \right]^2 \\ \Rightarrow -\frac{j\lambda}{4\pi} \ln \rho_i &= \sum_{k=i}^{i_{max}} d_k^i (N_k - N_{k+1}) \end{aligned} \quad (\text{A14})$$

Equation (A14) can be reformulated as a matrix equation in the following manner. In this formulation, the refractive index at radial positions beyond the imaging region ($r > i_{max}$) is assumed to be equal to n_0 . This assumption is based on the fact that those regions are sufficiently distant from the area irradiated by USPL, and therefore any refractive index modulation induced by the irradiation can be regarded as negligible.

$$\begin{aligned} & \frac{-j\lambda}{4\pi} \ln \begin{bmatrix} \rho_1 \\ \rho_2 \\ \vdots \\ \rho_{i_{max}-1} \\ \rho_{i_{max}} \end{bmatrix} \\ &= \begin{bmatrix} a_1 & b_2^1 & \dots & b_{i_{max}-1}^1 & b_{i_{max}}^1 \\ 0 & a_2 & \dots & b_{i_{max}-1}^2 & b_{i_{max}}^2 \\ \vdots & \vdots & \ddots & \vdots & \vdots \\ 0 & 0 & \dots & a_{i_{max}-1} & b_{i_{max}}^{i_{max}-1} \\ 0 & 0 & \dots & 0 & a_{i_{max}} \end{bmatrix} \begin{bmatrix} N_1 \\ N_2 \\ \vdots \\ N_{i_{max}-1} \\ N_{i_{max}} \end{bmatrix} - n_0 \begin{bmatrix} d_{i_{max}}^1 \\ d_{i_{max}}^2 \\ \vdots \\ d_{i_{max}}^{i_{max}-1} \\ d_{i_{max}}^{i_{max}} \end{bmatrix} \end{aligned} \quad (\text{A15})$$

Here, the following shorthand notations are used for the matrix elements:

$$\begin{aligned} a_i &\equiv d_i^i \\ b_j^i &\equiv d_j^i - d_{j-1}^i \end{aligned} \quad (\text{A16})$$

The refractive index profile can be retrieved by isolating the first term in Eq. (A15) and applying the inverse matrix.

6. Overview of Shadowgraphy and Its Limitations

In the main text, shadowgraphy was introduced as a conventional technique for measuring the imaginary component of the refractive index in the vicinity of a laser-induced filament. This section provides a concise overview of this method and discusses its inherent limitations.

Shadowgraphy relies on the quantitative relationship between a material's absorption coefficient and the transmittance of probe light, as described by the Beer–Lambert law:

$$\frac{I_1}{I_0} = \exp\left(-\int \alpha_x dx\right) \quad (\text{A17})$$

where the probe beam is assumed to propagate along the x -axis, and α_x denotes the absorption coefficient at each x coordinate. I_0 and I_1 represent the incident and transmitted light intensities, respectively. Assuming cylindrical symmetry of the filament, the integral in Eq. (A17) can be numerically evaluated by discretizing the axisymmetric distribution of α along the beam path, as detailed in the main text. Under this configuration, the spatial distribution of the imaginary part of the refractive index k can be estimated via the general relation $\alpha = 2\omega k/c$, where ω is the angular frequency of the probe light and c is the speed of light.

The limitations of shadowgraphy become particularly evident when the probe light intensity is insufficient. Figure A7(a) demonstrates this effect by comparing the spatial distribution of the imaginary component of the refractive index near a filament induced by a 2-ps USPL, under three distinct probe intensity conditions: high, medium, and low. As shown in the spatial maps, the retrieved profiles are highly sensitive to the probe intensity. For a more quantitative analysis, panel (b) presents the refractive index values along the filament axis, while panel (c) shows the transverse distributions at the sample interface ($z = 0$). The results exhibit a consistent trend: lower probe intensities lead to a progressive underestimation of the measured refractive index values.

This effect is most pronounced in panel (c). Under sufficiently high probe intensity, the reconstructed radial profile of the imaginary refractive index component assumes a Gaussian-like shape, mirroring the spatial intensity profile of the USPL and thus reflecting the expected refractive index modulation (see the main text). However, as the probe intensity decreases, this correspondence deteriorates: the reconstructed values near the filament axis fall below those of the surrounding region, resulting in an unphysical distribution. From a physical perspective, the central region of the filament should experience the highest laser intensities, and therefore, exhibit the greatest refractive index

modulation. The observed deviation under low probe intensity strongly suggests a measurement artifact, rather than a genuine physical feature.

This discrepancy can be qualitatively explained by the limited precision in determining the transmittance ratio in Eq. (A17) at low probe intensities. Specifically, when the incident intensity I_0 becomes small, the signal-to-noise ratio for measuring the transmittance I_1/I_0 decreases, leading to increased uncertainty and systematic underestimation in the derived absorption coefficient, and consequently, the imaginary refractive index.

In contrast, the method proposed in this study is intrinsically resistant to such degradation in measurement accuracy arising from variations in probe intensity. This robustness stems from the fact that the probe intensity affects only the amplitude A in Eq. (2), while the refractive index-related parameters Ψ and Δ remain unaffected. Consequently, the proposed approach enables more reliable extraction of the refractive index, even under suboptimal probe intensity conditions.

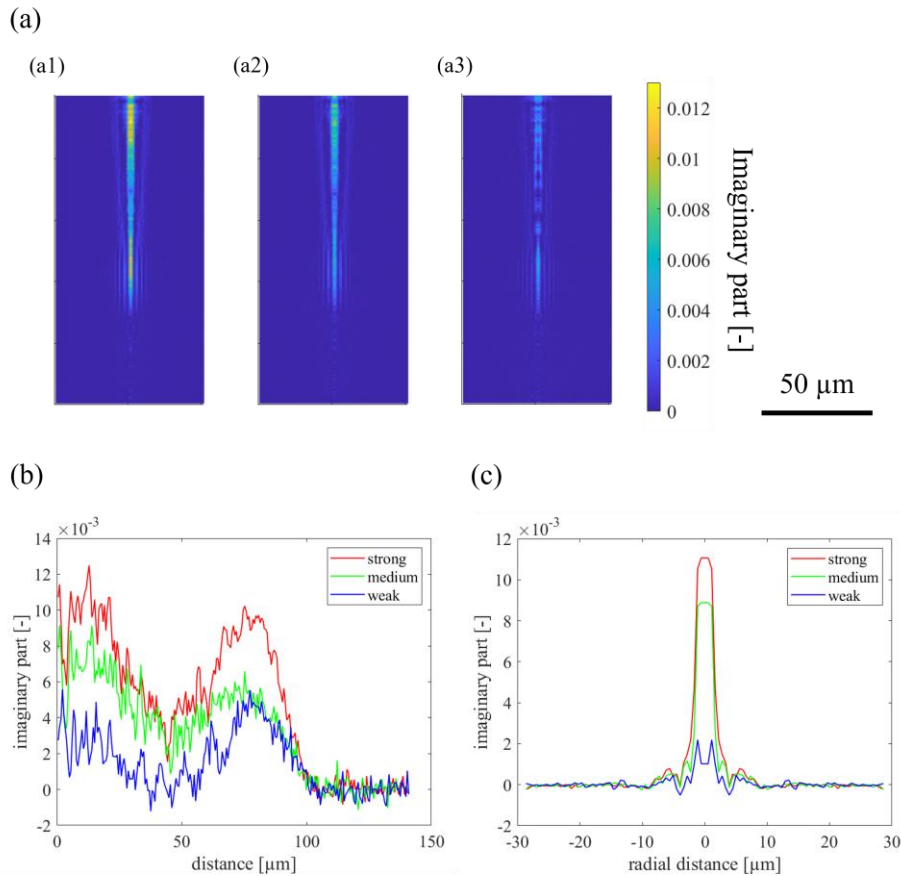


Fig. A7 Effect of Probe Intensity on Shadowgraphy-Based Estimation of Imaginary Refractive Index: (a1–a3) spatial distributions under high, medium, and low probe intensities, respectively; (b) longitudinal profiles along the filament axis; and (c) transverse profiles at the sample interface ($z = 0$).

7. Overview of the Drude Model Used for Real-Part Estimation

This section provides an outline of the Drude model applied to estimate the real part of the refractive index in the main text. This model offers a classical description of the dynamics of photoexcited electrons induced in a dielectric medium. The complex refractive index N is given by the following expression:

$$N = \sqrt{n_0^2 - \frac{e^2 n_e}{m_e \epsilon_0} \frac{1}{\omega^2 + i\omega\nu}} \quad (\text{A18})$$

The parameters appearing in Eq. (A18), along with their physical meanings and typical values, are summarized in Table A2.

Table A2 Physical parameters used in the Drude model.

Notation	Description	Typical value
N	Complex refractive index	N/A
n_e	Excited electron density	N/A
ν	Electron collision frequency	$1 \times 10^{15} - 1 \times 10^{16}$ [1/s]
n_0	Refractive index of pristine fused silica	1.461 [-]
ω	Laser pulsation	3.66×10^{15} [rad/s]
e	Elementary charge	1.602×10^{-19} [C]
m_e	Electron mass	9.109×10^{-31} [kg]
ϵ_0	Vacuum permittivity	8.854×10^{-12} [F/m]

The Drude model is particularly suited to estimating the real part of the refractive index due to its characteristic prediction that both the real and imaginary parts vary monotonically with the excited electron density. This relationship is illustrated in Fig. A8: panels (a1) and (a2) show the calculated imaginary and real parts, respectively, as functions of n_e at a representative collision frequency of $\nu = 5 \times 10^{15} \text{ s}^{-1}$. As n_e increases, the imaginary part increases monotonically, while the real part decreases monotonically. This monotonic dependence establishes a one-to-one correspondence under a fixed ν : a given imaginary component uniquely determines n_e , which in turn determines a unique real part (see the green dashed arrows in panels (a1) and (a2)). This mapping is visualized in panel (a3), and its variation with respect to ν is shown in panel (b).

In the main text, this property was leveraged to estimate the real part of the refractive index from experimentally measured values of the imaginary part. The resulting estimates are compared with independent experimental measurements. Since the estimated real part depends on the assumed value of ν , as discussed previously, agreement between the

estimated and measured values—when using ν values consistent with prior literature—supports the validity of the proposed experimental method. Nevertheless, it should be noted that the applicability of this method is limited to regimes in which the optical response of the excited region is adequately described by the Drude model. To date, no numerical model accurately captures carrier dynamics across the full temporal range—from initial excitation to subsequent relaxation. Therefore, any model-based interpretation should be made with appropriate caution regarding these inherent limitations.

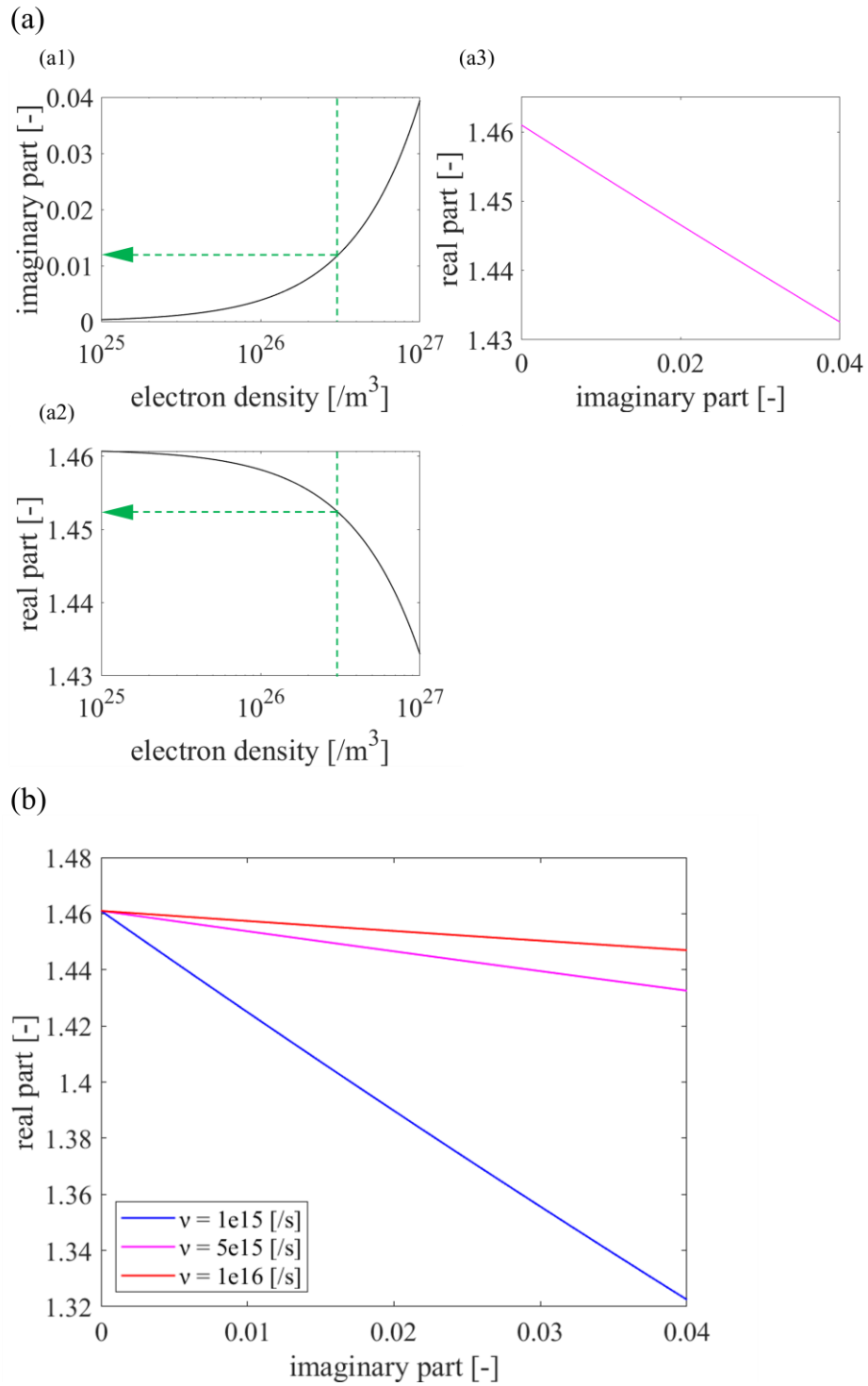


Fig. A8 Drude Model-Based Relationship Between Excited Electron Density and Complex Refractive Index: (a1, a2) imaginary and real parts as functions of electron density at $\nu = 5 \times 10^{15} \text{ s}^{-1}$; (a3) one-to-one mapping between imaginary and real parts under fixed ν ; (b) dependence of this mapping on the collision frequency ν .